Nanoscale

PAPER

View Article Online
View Journal | View Issue

Cite this: *Nanoscale*, 2015, **7**, 6545

New surface radiolabeling schemes of super paramagnetic iron oxide nanoparticles (SPIONs) for biodistribution studies†

Prakash D. Nallathamby,*[a,b,d] Ninell P. Mortensen,[b] Heather A. Palko,[a,c] Mike Malfatti,[c] Catherine Smith,[a] James Sonnett,[a] Mitchel J. Doktycz,[b] Baohua Gu,[b] Ryan K. Roeder,[d] Wei Wang*[b] and Scott T. Retterer*[b]

Nanomaterial based drug delivery systems allow for the independent tuning of the surface chemical and physical properties that affect their biodistribution *in vivo* and the therapeutic payloads that they are intended to deliver. Additionally, the added therapeutic and diagnostic value of their inherent material properties often provides extra functionality. Iron based nanomaterials with their magnetic properties and easily tailorable surface chemistry are of particular interest as model systems. In this study the core radius of the iron oxide nanoparticles (NPs) was 14.08 ± 3.92 nm while the hydrodynamic radius of the NPs, as determined by Dynamic Light Scattering (DLS), was between 90–110 nm. In this study, different approaches were explored to create radiolabeled NPs that are stable in solution. The NPs were functionalized with polycarboxylate or polyamine surface functional groups. Polycarboxylate functionalized NPs had a zeta potential of −35 mV and polyamine functionalized NPs had a zeta potential of +40 mV. The polycarboxylate functionalized NPs were chosen for *in vivo* biodistribution studies and hence were radiolabeled with ^{14}C, with a final activity of 0.097 nCi mg^{-1} of NPs. In chronic studies, the biodistribution profile is tracked using low level radiolabeled proxies of the nanoparticles of interest. Conventionally, these radiolabeled proxies are chemically similar but not chemically identical to the non-radiolabeled NPs of interest. This study is novel as different approaches were explored to create radiolabeled NPs that are stable, possess a hydrodynamic radius of <100 nm and most importantly they exhibit an identical surface chemical functionality as their non-radiolabeled counterparts. Identical chemical functionality of the radiolabeled probes to the non-radiolabeled probes was an important consideration to generate statistically similar biodistribution data sets using multiple imaging and detection techniques. The radiolabeling approach described here is applicable to the synthesis of a large class of nanomaterials with multiple core and surface functionalities. This work combined with the biodistribution data suggests that the radiolabeling schemes carried out in this study have broad implications for use in pharmacokinetic studies for a variety of nanomaterials.

Received 1st November 2014,
Accepted 21st February 2015

DOI: 10.1039/c4nr06441k

www.rsc.org/nanoscale

[a]*Battelle Center for Fundamental and Applied Systems Toxicology, Battelle Memorial Institute, Columbus, OH 43201, USA*
[b]*Biological and Environmental Sciences Divisions, Oak Ridge National Laboratory, Oak Ridge, TN 37831, USA. E-mail: pnallath@nd.edu, retterert@ornl.gov, wangw@ornl.gov*
[c]*Biosciences and Biotechnology Division, Physical and Life Sciences, Lawrence Livermore National Laboratory, Livermore, CA 94550, USA*
[d]*Department of Aerospace and Mechanical Engineering; Bioengineering Graduate Program, University of Notre Dame, Notre Dame, IN 46556, USA*

† Electronic supplementary information (ESI) available: (S1) High-Resolution Transmission Electron Microscopy (HRTEM) image of iron oxide nanoparticles, (S2) Superconducting Quantum Interference Device (SQUID) measurement of magnetization of super paramagnetic iron oxide nanoparticles, (S3) Fourier Transform Infrared Spectroscopy (FT-IR) spectra of Fe-Si-COO^- synthesised using Grignard reagents (S4) FT-IR spectra of iron oxide nanoparticles silanized with commercially available N-[(3-Trimethoxysilyl)propyl]ethylenediamine triacetic acid tripotassium salt, (S5) Synthesis of hyperbranched amine functionalized iron oxide nanoparticles from amino propyl triethyl silane functionalized iron nanoparticles using ethyleneimine as an initiator and polymerizing agent. See DOI: 10.1039/c4nr06441k

Introduction

Before drug candidates are approved for clinical trials in human subjects, their toxicity profile and pharmacokinetic data has to be assessed in *in vitro* tissue and *in vivo* animal models.[1–4] It is not uncommon for candidates to pass this screening process successfully only to exhibit poor specificity, solubility and distribution *in vivo*.[5–9] Such failures, deep in the clinical testing process, results in tremendous research and development costs that are ultimately passed on to consumers through the limited number of drugs that do make it to the market. It is possible to lower the costs of development for promising drug agents to the clinical trial phase by creating drug formulations that improve efficacy and reduce side effects through targeted delivery. Nanomaterial drug delivery systems

have generated significant interest because of the potential to tune targeting moieties and therapeutic payload independently while capitalizing on the inherent material properties of the systems. They have found multiple uses in applications for drug delivery,[10] theranostics,[11,12] biomedical imaging,[13–16] and as therapeutic agents.[17,18] Nanomaterial systems can have diffusion kinetics that approach the molecular level while allowing the addition of cell specific targeting molecules and possible multi-therapeutic agents due to flexible surface functionalization schemes.[19–22] Nanomaterial systems can also facilitate multimodal tracking or imaging *in vivo*, which can dramatically improve the accuracy of the biostatistics collected during pre-clinical trials.

In this study we used iron oxide based superparamagnetic nanomaterials as a model system (Fig. S1 and S2†), since they are already prevalent in pharmaceutical and biomedical research.[23,24] Their inherent superparamagnetic properties make them useful as (a) MRI contrast agents, (b) targeted drug delivery agents, (c) targeted therapeutic agents through magnetic hyperthermia, and (d) as gene transfection agents.[25–28] This broad range of applications is made possible by the fact that the surface of iron oxide nanomaterials can be easily modified to a wide variety of chemical functionalities by using a range of commercially available organosilane compounds.[29,30] Further, the radiolabeling schemes carried out on iron oxide cores, which are not as chemically inert as gold or silica cores, are easily transferrable and broadly applicable to a diverse range of nanomaterials used for biomedical applications.

Biological efficacy of nanomaterial drug delivery systems depends upon the material distribution and rate of bio-absorption *in vivo*, which in turn, is also dependent on the route of delivery.[31,32] Intravenous injection or inhalation are the preferred routes of administration.[33] Stimulated particle deposition studies using the industry standard Anderson Cascade Impactor clearly demonstrate, that a 200–400 nm particle size will leads to deposition in the alveoli and interstitium. Particle sizes below 200 nm will pass through the alveoli and be absorbed into the bloodstream.[34,35] Previous work conducted by our collaborators had clearly demonstrated the need for iron oxide particle sizes of <150 nm for efficient dose delivery through a nebulizer.[33] Thus we set the targeted hydrodynamic radius of the magnetic nanoparticles in this study to be 100 nm. Three different reaction schemes that created $-COO^-$ groups on the surface of the nanoparticles were developed. The $-COO^-$ groups create charge–charge separation among nanoparticles to prevent aggregate formation and enable the reaction schemes that allow for the incorporation of ^{14}C radio isotopes into the carbon backbone of the surface functional groups. The most stable nanomaterials system designed in this study was water dispersed iron oxide nanoparticles (~10 nm) with branched carboxylic acid ($-COO^-$) functional groups. Once the size and chemical stability of nanoparticles was optimized in solution, the *in vitro* nanotoxicity of non-radio labelled nanoparticles was determined using RAW 264.7 macrophage cells and C10 mouse lung epithelial cells. The biodistribution of the radiolabeled NPs was then assessed *in vivo* in a mouse model system.

The radiolabeling approach used in this study was unique, as the radiolabeled nanomaterials were the same shape and surface chemistry as the non-labelled materials that they were intended to mimic. In addition, the differences in size distributions were not statistically significant. The nanoparticles synthesized in this work have implications for use in different biological applications. Taken together, the approach described here points towards the utility in using advanced nanomaterial synthesis strategies in coordination with multiple imaging and characterization tools to develop a more complete, multi-scale picture of nanomaterial distribution and toxicity.

Results and discussion

Synthesis of stably dispersed iron oxide nanoparticles

Scanning Electron Microscopy (SEM) data indicated an iron oxide NP core size of 14.08 ± 3.92 nm (Fig. 1A and B). The Fourier Transform Infrared Spectroscopy (FT-IR) spectrum shows the typical broad peak associated with –OH groups between 3300–3500 cm^{-1} (Fig. 1C). Dynamic Light Scattering (DLS) measurements of iron oxide NPs prepared by the co-precipitation method in water indicated agglomerate sizes of 1110.9 ± 483.3 nm (Fig. 1D). Iron oxide agglomerates in the micron size range severely limits their suitability for biomedical applications. Aggregates in this size range are too big to aerosolize and clog intravenous needles depending on the flow rate of the solution.[36] This in turn will affect the rate and net dose delivered.

Iron oxide NPs are super paramagnetic and naturally tend to aggregate in solution. An effective way to reduce aggregation of nanoparticles is to increase the solubility of individual nanoparticles in solution by increasing the electrical double layer on the surface of the nanoparticles or by adding stabilizers and surfactants to the solution. It is possible to increase the zeta potential of the nanoparticles in solution by creating ionic functional groups on the surface of the nanoparticles. For example this can be done by either creating $-COO^-$ or $-NH_4^+$ on the surface of the nanoparticles.[22] We carried out three different reaction schemes to create $-COO^-$ groups on the surface of the NPs. The synthesis of $-COO^-$ groups on the surface of NPs using the Grignard method did not yield stably dispersed nanoparticles (Fig. S3†). But the synthesis of $-COO^-$ groups on the surface of NPs through the base hydrolysis of nitrile (CN) groups yielded stable solutions of nanoparticles through two different reaction schemes.

In the first reaction scheme (Fig. 2A), iron oxide NPs were silanized with chloromethyltriethoxylsilane. The chlorine in chloromethyltriethoxysilane functionalized iron oxide NPs were substituted by iodine using the Finkelstein reaction. The iodine in the iodinated iron nanoparticles were replaced with a nitrile group (C≡N) by refluxing the NPs in ethanol in the presence of potassium cyanide to get C≡N functionalized iron

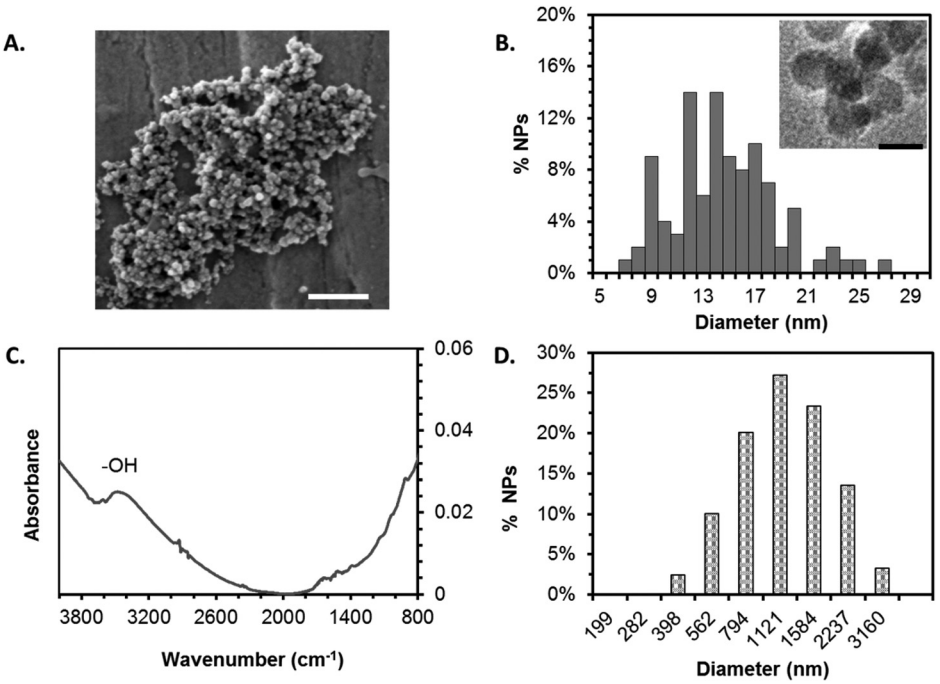

Fig. 1 Chemical and physical characterization of iron oxide nanoparticles. (A) SEM image of iron oxide nanoparticles dispersed in water. Scale bar = 100 nm. (B) Core size distribution of iron oxide NPs as determined by TEM was 14.08 ± 3.92 nm. Scale bar = 20 nm. (C) FT-IR spectra of iron oxide showed broad lines due to –OH between 2500–3300 cm^{-1}. (D) The hydrodynamic diameter of iron oxide NPs in water was determined by DLS to be 1110.9 ± 483.3 nm.

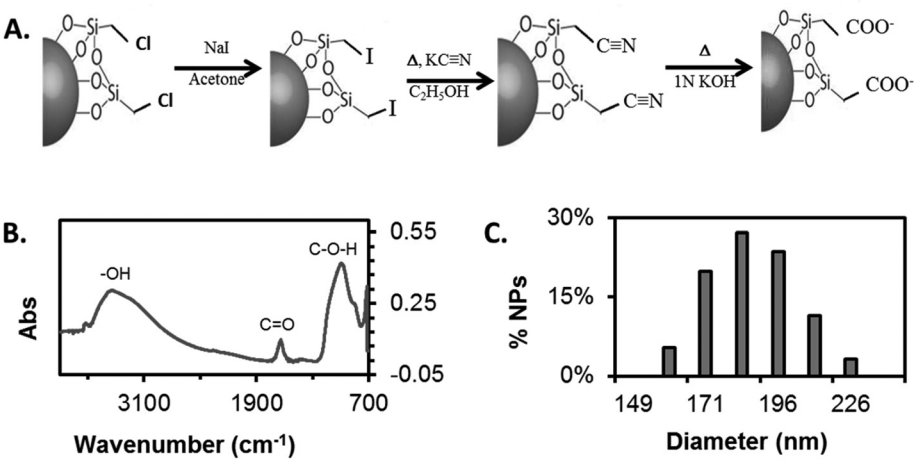

Fig. 2 (A) Schematic of the chemical reactions required to convert the chlorine group on chloromethyltriethoxysilane coated iron oxide NPs to carboxylate functional group. The carboxylated NPs were designated as Fe–Si–COO^- NPs. (B) FT-IR spectra of acid treated Fe–Si–COO^- NPs confirms the presence of –COOH groups on the surface of NPs through peaks at 930 cm^{-1} (C–O–H) , 1640 cm^{-1} (C═O) and a broad peak between 3200–3500 cm^{-1} (–OH). (C) The hydrodynamic diameter of Fe–Si–COO^- NPs in water as determined by DLS was 187.4 ± 20.1 nm.

oxide NPs (Fe–Si–CN NPs). The C≡N functional groups on the Fe–Si–CN NPs were converted to $–COO^-$ functional group by base hydrolysis under reflux. The iron oxide NPs with carboxylate groups were designated Fe–Si–COO^- NPs. FT-IR spectra was used to confirm the presence of $–COO^-$ groups on the surface of the Fe–Si–COO^- NPs. Multiple peaks of medium to strong signal strength were located at 1000–1100 cm^{-1} and this was correlated to the –C–OH chemical bonds. A strong peak between 1600–1700 cm^{-1} can be correlated to the C═O bond and broad peak around 3300 cm^{-1} was correlated to the –OH group (Fig. 2B). Zeta potential of Fe–Si–COO^- NPs was measured at −34.73 ± 2.57 mV using a BrookHaven 90Plus/BI-MAS. The high negative charge on the surface of the NPs significantly enhanced stability of the NPs dispersed in water.

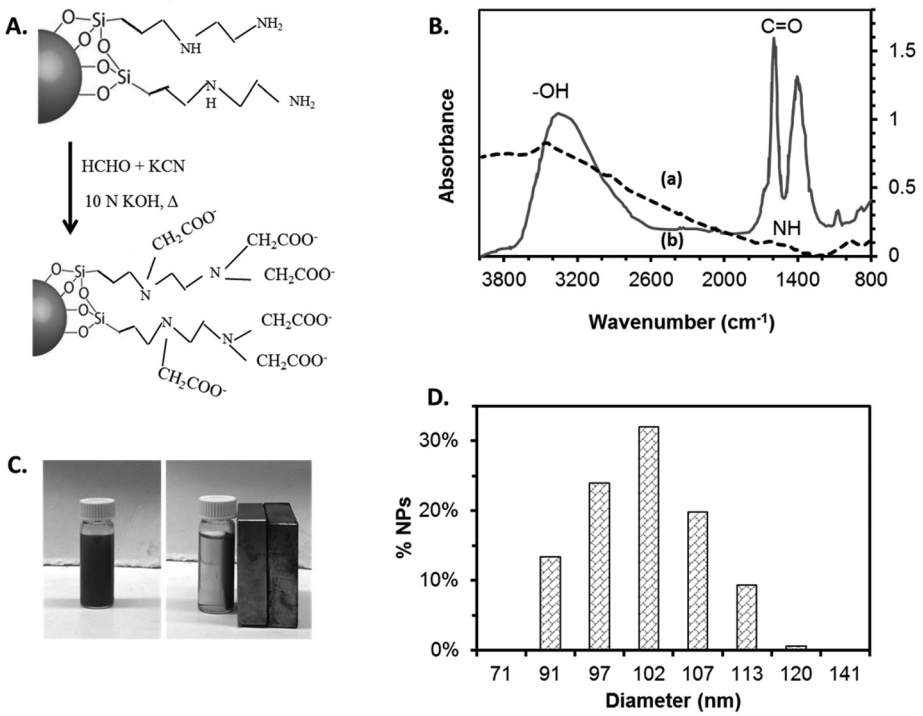

Fig. 3 (A) Schematic of the chemical reactions required to convert the ethylenediamine functional groups on iron oxide NPs to carboxylate functional group. The carboxylated NPs were designated as Fe–Si–$(COO^-)_3$ NPs. (B) FT-IR spectra of (a) Fe–Si–diamine NPs confirmed the presence of amine groups by the presence of a small broad peak between 1000–1250 cm^{-1} corresponding to C–N stretch and peaks at 1650–1580 cm^{-1}/3300–3500 cm^{-1} corresponding to –NH bending. (b) FT-IR spectra of Fe–Si–$(COO^-)_3$ NPs confirmed the presence of –COOH groups on the surface of NPs through strong peaks at 1580 cm^{-1} and 1395 cm^{-1} (C═O) and a broad peak between 3200–3500 cm^{-1} (–OH). (C) The superparamagnetic nature of Fe–Si–$(COO^-)_3$ NPs dispersed in water in the presence of a magnet. (D) The hydrodynamic diameter of Fe–Si–$(COO^-)_3$ NPs in water as determined by DLS was 101.7 ± 19.4 nm.

However the DLS measurements indicated Fe–Si–COO^- NPs had a hydrodynamic diameter of 187.4 ± 20.1 nm, which was twice the target diameter (Fig. 2C).

In the second reaction scheme (Fig. 3A), iron oxide NPs were silanized with ethylenediamine. The ethylene diamine functional groups on Fe–Si–diamine NPs were converted to ethylenediaminetriacetate groups using a modified synthesis of EDTA (Fig. 3A).[37] FT-IR spectra of Fe–Si–Diamine and Fe–Si–$(COO^-)_3$ NPs showed the evolution of formation of –COO^- groups which replace the hydrogen in the amine groups (Fig. 3B). FT-IR spectra of Fe–Si–diamine NPs confirmed the presence of amine groups by the presence of a small broad peak between 1000–1250 cm^{-1} corresponding to C–N stretch. Peaks at 1650–1580 cm^{-1} and 3300–3500 cm^{-1} corresponded to –NH bending (Fig. 3B-a). After complete conversion of ethylene diamine on Fe–Si–Diamine NPs to ethylenediamine triacetate, there were strong peaks at 1650–1500 cm^{-1} and 1210–1320 cm^{-1} from –COOH vibration and a broad peak at 2500–3300 cm^{-1} from –OH stretching,[38,39] while the broad peak between 3300–3500 cm^{-1} due to N–H stretching disappears (Fig. 3B-b). FT-IR spectra of Fe–Si–$(COO^-)_3$ NPs was identical to the FT-IR spectra of iron oxide NPs silanized with commercially available *N*-[(3-trimethoxysilyl)propyl] ethylenediamine triacetic acid (Fig. S4†) thus confirming our reaction scheme was successful. The –COOH functionalized nanoparticles were extremely well dispersed in solution and resistant to aggregation. The zeta potential of Fe–Si–$(COO^-)_3$ NPs was measured at −37.73 ± 2.39 mV which explained the highly stable dispersion of NPs in water (Fig. 3C). The hydrodynamic diameter of Fe–Si–$(COO^-)_3$ NPs as determined by DLS measurements indicated sizes of 101.73 ± 19.4 nm (Fig. 3D). This size range has been shown to be ideal for both intravenous mode of delivery and delivery through a nebulizer. Therefore, Fe–Si–$(COO^-)_3$ NPs were chosen for further biomedical assessments using *in vitro* toxicity assays and *in vivo* biodistribution studies.[40]

In vitro toxicity assays

The chemical toxicity of non-labelled Fe–Si–$(COO^-)_3$ NPs was tested against two cell lines. The cell lines used were C10 murine lung epithelial cells and RAW 264.7 macrophage cells.[41–44] The cell lines were chosen based on the two widely used routes of drug delivery: (a) Intravenous or (b) pulmonary. If inhalation is the mode of delivery, epithelial cells in the nasal tract and lungs will be the first to be exposed to the nanoparticles. C10 murine lung epithelial cells have been widely referenced in literature as an *in vitro* model system for studying the cytotoxicity of nanoparticles on lung cells.[41,42] If intravenous delivery is the mode of delivery then a possible

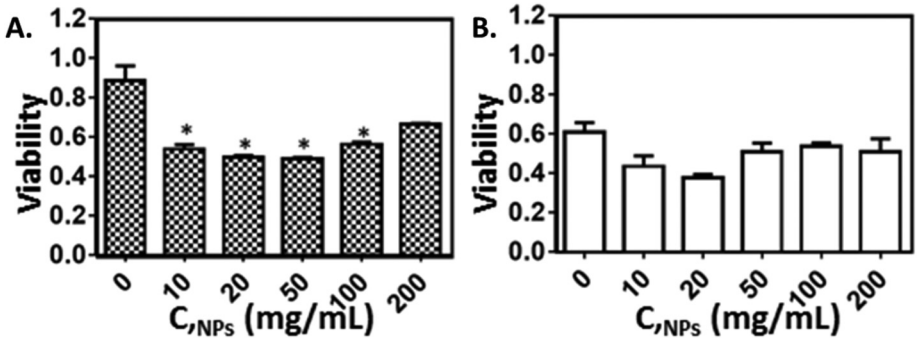

Fig. 4 *In vitro* toxicity assays were performed using Fe–Si–$(COO^-)_3$ NPs to assess cytotoxicity. *In vitro* model cell cultures were tested for cell metabolic activity, 24 hours post-incubation with NPs, using MTT assay for (A) RAW 264.7 cells and (B) C10 cells. The cell population incubated with highest concentration of NPs did not show any increased toxicity as when compared to the cell population incubated with the lowest concentration of NPs. *$p < 0.05$ *vs.* control (paired *t*-test).

immune response could be launched by white blood cells in the blood. RAW 264.7 macrophages have been used extensively to detect phagocytosis of nanoparticles in a size, shape and chemical functionality dependent manner to assess hemotoxic effects of nanoparticles.[43,44] Therefore, C10 lung epithelial cells and RAW 264.7 macrophage cells were chosen to assess *in vitro* cytotoxicity of non-radiolabelled NPs. The viability of the cell lines was assessed using MTT assay at 24 hour's post-exposure to nanoparticles as described previously.[14,45]

The MTT assay is a colorimetric assay for measuring the activity of enzymes that reduce MTT to formazan dyes, giving the cell medium a purple color. The absorbance of this colored solution is quantified at 490 nm. These reductions take place only when reductase enzymes are active, and therefore conversion was used as a measure of viable (living) cells. The mitochondrial activity and thereby the ability of the cell to respire for RAW 264.7 macrophage cells (Fig. 4A) and C10 lung epithelial cells (Fig. 4B) were tested 24 hours after incubation with NPs using MTT assay. Five concentrations were utilized ranging from 0–200 μg mL^{-1} of NPs. These concentrations were chosen in order to cover all possible dosage ranges for both inhalation and intravenous modes of delivery. All experiments were performed in triplicate. Cells incubated in the absence of NPs were the control population. The control cells exhibited the highest viability. However among the cells dosed with NPs there was no clear trend pointing to a dose dependent toxicity effect for the range of dosages analysed. This indicated that the NPs were not demonstrating a dose dependent ability to compromise the ability of the cells to respire and thereby were not affecting cell metabolic activity. The *in vitro* toxicity assays indicated that the NPs were non-toxic to the test cell population for the concentration ranges tested.

Synthesis of chemically identical radiolabeled iron oxide nanoparticles

Once *in vitro* toxicity assays showed that Fe–Si–$(COO^-)_3$ NPs were not cytotoxic, the mouse model system was chosen to track the biodistribution profile of radiolabeled Fe–Si–$(COO^-)_3$ NPs. Radiolabelling NPs allows NPs to be tracked in tissue samples with high sensitivity using a ultra-sensitive Accelerator Mass Spectrometer (AMS). AMS counts isotopes independent of their radioactive decay; the radioisotope of interest is measured relative to a stable isotope of the same element which results in a mass ratio.[46–49] Common radiolabeling techniques include formation of an amide bond between the $-COO^-$ group on the surface of the nanoparticles and a radiolabeled amine compound or through the use of click chemistry.[50,51] These more conventional techniques alter the surface chemistry, which in turn will affect the absorption, distribution, metabolism and excretion profiles of these NPs (potential drug carriers) *in vivo*. This will result in lost time and expenses collecting results, which cannot accurately predict the pharmacokinetics of the non-radiolabeled NPs *in vivo*. Other commonly used methods include chelating radiolabels on the surface of the NPs or adsorbing radiolabels to the surface of the NPs.[47,52] However, there is the possibility that chelated or adsorbed radiolabels will disassociate from the NPs in physiological conditions. In such cases, the radiolabel distribution measured would not be indicative of the biodistribution of NPs.[53,54] Fe–Si–$(COO^-)_3$ NPs were radiolabeled using reaction schemes that allowed us to make radiolabeled NPs that were chemically identical to the non-radiolabeled nanoparticles and which gave us the most stable nanoparticles in solution. We chose ^{14}C as the radiolabel in this study because it afforded us considerable flexibility in designing our reaction schemes. Further, the majority of biological applications of AMS use ^{14}C as the radiolabel because the majority of biological samples of interest contain carbon. Additionally, ^{14}C is a beta emitter with a ($t_{1/2}$ = 5730 years) that can be easily detected at ultra-low concentrations (10^{-18}) using accelerator mass spectrometry.

To incorporate ^{14}C into the carboxylate functional group (Fig. 5A), the Fe_3O_4 NPs were first silanized with *N*-[3-(trimethoxysilyl)propyl]ethylenediamine (Si–Diamine) and designated as Fe–Si–Diamine. Each functional diamine group has

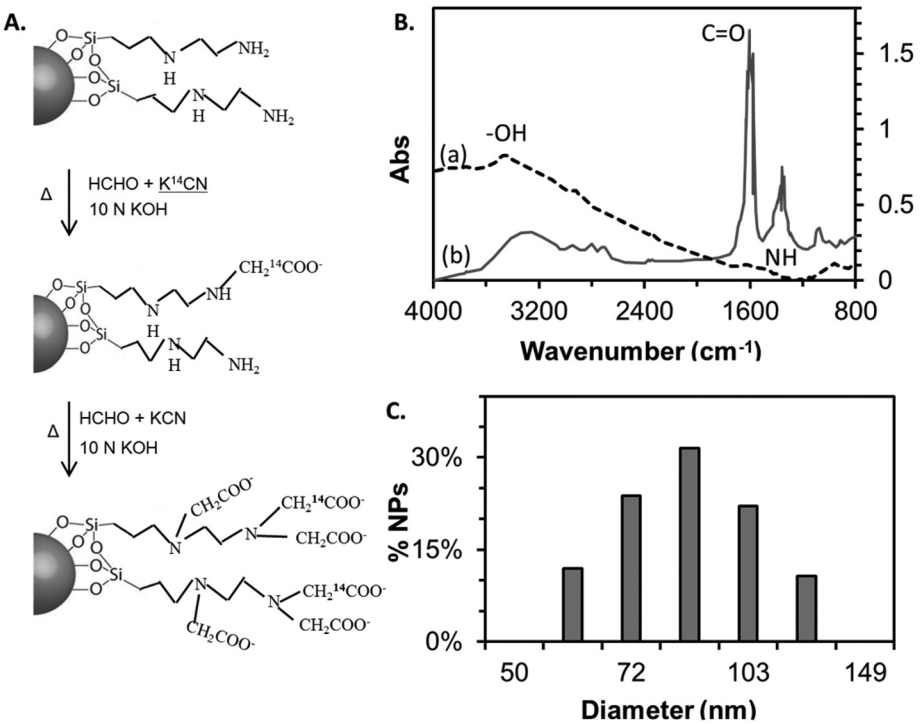

Fig. 5 (A) Schematic of the chemical reactions required to convert the ethylenediamine functional groups on iron oxide NPs to carboxylate functional group with ^{14}C incorporated in them. The carboxylated NPs were designated as ^{14}C–Fe–Si–$(COO^{-})_3$ NPs. The specific radioactivity was 0.097 nCi/mg of NPs. (B) FT-IR spectra of (a) Fe–Si–diamine NPs and (b) ^{14}C–Fe–Si–$(COO^{-})_3$ NPs confirmed the presence of –COOH groups on the surface of NPs through strong peaks at 1605 cm^{-1} and 1342 cm^{-1} (C═O) and a broad peak between 3200–3500 cm^{-1} (–OH). (C) The hydrodynamic diameter of ^{14}C–Fe–Si–$(COO^{-})_3$ NPs in water as determined by DLS was 87.11 ± 7.83 nm.

three active sites in total, which can react to undergo a substitution reaction to incorporate a total of three $-CH_2COO^{-}$ groups per organic silane. The reaction employed was adapted from the commercial synthesis of EDTA from ethylenediamine.[37] But this is the first time that the reaction has been optimized to occur on the surface of iron oxide nanoparticles. We achieved radioactivity of 0.097 nCi mg^{-1} of NPs used for the *in vivo* biodistribution study. The radioactivity was tunable up to 100 nCi mg^{-1} of NPs by using a ^{14}C source with higher specific radioactivity (5×10^6 nCi). The radiolabeled Fe–Si–$(COO^{-})_3$ NPs were designated as ^{14}C–Fe–Si–$(COO^{-})_3$ NPs. FT-IR spectra confirmed chemical alikeness with the non-radiolabeled NPs (Fig. 5B) and DLS indicated a hydrodynamic diameter of 87.11 ± 7.83 nm (Fig. 5C).

After the ^{14}C–Fe–Si–$(COO^{-})_3$ NPs were purified and characterized, the stability of nanoparticles in solution and under physiological conditions was determined. Characterizing the stability of radiolabels bound to the surface of the nanoparticles under physiological conditions is important, as any instability will result in free radio labels in solution, which in turn will give rise to false biodistribution profiles *in vivo*. The Stability of radiolabels on Fe_3O_4–Si–$(^{14}COO^{-})$ in saline and fetal bovine serum at room temperature was monitored for a time period of 48 hours (Fig. 6A). There was no detectable

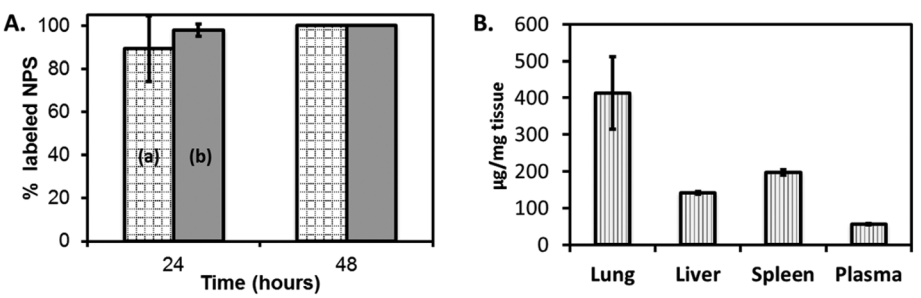

Fig. 6 (A) The radiolabels on ^{14}C Fe–Si–EDTA NPs in (a) saline and (b) fetal bovine serum were determined to be stable for at least 48 hours. (B) 0.15 mg of the ^{14}C Fe–Si–EDTA NPs were administered intravenously through the tail vein as one dose. The *in vivo* biodistribution was determined 30 minutes after the final dose was delivered by using AMS to determine the $^{14}C/^{12}C$ ratio in tissue from different organs.

radioactivity in the supernatant nor was there any significant loss in radioactivity in the nanoparticle fraction. This indicated that the radiolabels were linked stably to the nanoparticles surface in physiological conditions.

In vivo biodistribution of radiolabeled NPs

Once the stability of radiolabeled NPs in physiological medium was confirmed, 0.15 mg of ^{14}C Fe–Si–EDTA NPs nanoparticles were administered intravenously through the tail in 100 μl of saline followed by a 50 μl saline flush. The *in vivo* biodistribution in mouse animal model was determined 30 minutes after the final dose was delivered. AMS was used to analyse the biodistribution of ^{14}C Fe–Si–EDTA NPs in tissue samples from different organs of the mouse animal model. The nanoparticles were found distributed throughout the mouse animal model with a higher concentration in lungs. This non-specific distribution of the ^{14}C Fe–Si–EDTA NPs can be directly correlated to the biodistribution of Fe–Si–EDTA NPs *in vivo* without complex statistical modelling. The biodistribution after intravenous delivery of NPs at 30 minutes is shown in Fig. 5. NPs were found in the phagocytic organs: lung (~400 μg mg^{-1}), liver (~150 μg mg^{-1}) and spleen (~200 μg mg^{-1}). NPs were also observed in the blood plasma (~50 μg mL^{-1}) (Fig. 6B).

The observed biodistribution in Fig. 6 was consistent with other studies that detailed biodistribution of iron oxide nanoparticles. Nanoparticles are known to be rapidly engulfed by macrophages after administration for accumulation in macrophage rich organs (liver, spleen, and lung).[55,56] The higher concentration of NPs in the lung could be due to entrapment of the nanoparticles in the capillaries upon transport through the vasculature; this has been shown for larger NPs after injection.[57] This was an acute study aimed at showing that our unique radiolabeling scheme allowed us to create highly stable ^{14}C labelled nanoparticles with the same chemical properties as the non-labelled NPs of interest. Radiolabeling NPs allows for detection of NPs using an ultra-sensitive analytical tool like AMS, which has small sample requirements. The biodistribution data of the radiolabels can be confidently correlated to nanoparticle distribution *in vivo*. This negates the need for equivalency studies and affords a high level of statistical significance to the raw biodistribution data obtained, which allows for accurate biostatistics.

Conclusions

Branched organic chains with either –COO$^-$ functional group or –NH$_3$ functional groups (Fig. S5†) were synthesized *in situ* on the surface of iron oxide NPs for the first time, to yield highly stabilized, deagglomerated, ferromagnetic nano-fluids. This unique functionalization scheme allowed the hydrodynamic size of the magnetic iron oxide NPs clusters to be controlled between 75–100 nm. This was important, as this allowed for dual delivery modes *in vivo* without any change in formulation. The same formulation of NPs were administered *in vivo* either intra-venously as detailed in this study or by inhalation through a nebulizer.[33] The NPs were radiolabelled by incorporating ^{14}C directly into the carbon backbone of the organic molecules on the surface of the NPs. The radioactivity of the NPs was controlled at ~0.1 nCi mg^{-1}. The radioactivity was tuneable up to 100 nCi mg^{-1} of NPs by using a ^{14}C source with higher specific radioactivity of up to 5×10^6 nCi. By radiolabeling the NPs, low concentrations of NPs can be detected with high sensitivity using tools like ICP-MS and AMS, which can reach detection limits of 10^{-18} moles. The radiolabelling approach used in these studies was significant, as the probes had the same chemical properties as the non-labelled probes that they were intended to mimic. This was an acute study aimed at showing that our unique radiolabeling scheme allowed us to create highly stable ^{14}C labelled NPs with the same chemical properties as the non-labelled NPs of interest. This allows the *in vivo* biodistribution of NPs to be positively correlated to the *in vivo* biodistribution data of the radiolabels. This mitigates the need for equivalency studies and affords a high level of statistical significance to the raw biodistribution data obtained. Additionally, the low levels of radioactivity also permit long term pharmacokinetic studies without any systemic toxicity from the radiolabel itself. Furthermore, the magnetic core of the NPs allows for dual detection schemes using techniques such as magnetic particle imaging, which introduces redundancy into the biodistribution data. The NPs synthesized in this work have implications for use in different biological applications and the surface functionalization approach described is broadly applicable to the synthesis and functionalization of nanomaterials derived from other elements.

Experimental section

Reagents

NH_4OH(Sigma), $FeCl_3$ (Sigma-Aldrich), $FeSO_4{\cdot}7H_2O$ (Sigma-Aldrich), 15 MΩ milli-Q water, chloromethyltriethoxylsilane (Gelest), NaI (Fluka), KOH (Fluka), KCN (Fluka), K^{14}CN (ARC), *N*-[3-(trimethoxysilyl)propyl]ethylenediamine (Gelest), *N*-[(3-trimethoxysilyl)propyl]ethylenediamine triacetic acid tripotassium salt (Gelest), ethyleneimine (Fluka), acetic acid (VWR), 200 proof ethanol (VWR)

Synthesis and characterization of iron oxide nanoparticles

Iron oxide nanoparticles (NPs) with a core size of ~13–15 nm were synthesized by a standard co-precipitation method using NH_4OH as a reducing agent. 3.24 g of $FeCl_3$ (0.02 moles) was dissolved in 20 mL of water. 2.78 g of $FeSO_4{\cdot}7H_2O$ (0.01 moles) was dissolved in 5 mL of 2 M HCl. The Fe(II) in HCl and Fe(III) in water were mixed together so that the molar ratio of Fe(II)/Fe(III) was 1 : 2 in 25 mL solution. 250 mL of 8 M NH_4OH solution was added drop wise to the 1 : 2 :: Fe(II) : Fe(III) mixture under stirring. The solution turned from a clear brown to an opaque, black colloidal suspension in under 5 minutes. The colloidal suspension was allowed to stir overnight. The result-

ing iron oxide NPs were then magnetically separated and rinsed with milli-Q water 6 times and resuspended in 250 mL of milli-Q water.

Synthesis of Fe–Si–COO^- NPs

500 mg of iron oxide NPs in water was magnetically separated and resuspended in 100 mL of 90% ethanol. 1 mL of chloromethyltriethoxylsilane was dissolved in 9 mL of 90% ethanol and then added to the NPs solution under rapid stirring. The suspension was allowed to stir overnight to form Fe–Si–Cl NPs. After overnight stirring, the Fe–Si–Cl NPs were then magnetically separated and rinsed 3 times in milli-Q water followed by 3 rinses in acetone and finally resuspended in 100 mL of acetone saturated with NaI. The Fe–Si–Cl NPs are kept stirring overnight in acetone and NaI to allow for the displacement of Cl^- by I^- to yield Fe–Si–I NPs (Finklestein's reaction). After overnight stirring, the Fe–Si–I NPs were then magnetically separated and rinsed thrice in milli-Q water, followed by 3 rinses in ethanol and resuspended in 100 mL of ethanol. Excess KCN was then added to the Fe–Si–I NPs in ethanol and the solution was refluxed for 12 hours so that the nitrile (–CN) group displaced the iodine to yield Fe–Si–CN NPs. The Fe–Si–CN NPs were rinsed thrice in milli-q water, re-suspended in 1 N KOH and refluxed overnight. This converts the nitrile functional groups to $–COO^-$ functional groups and yielded Fe–Si–COO^- NPs.

Synthesis of Fe–Si–diamine NPs

500 mg of iron oxide NPs in water was magnetically separated and resuspended in 100 mL of 90% ethanol. 1 mL of *N*-[3-(trimethoxysilyl)propyl]ethylenediamine was dissolved in 9 mL of 90% ethanol and then added to the NPs under rapid stirring. The suspension was allowed to stir overnight. After overnight stirring, the NPs were then magnetically separated and rinsed in milli-Q water and resuspended in 100 mL of milli-Q water and designated as Fe–Si–diamine NPs.

Synthesis of Fe–Si–$(COO^-)_3$ NPs

N-[(3-Trimethoxysilyl)propyl]ethylenediamine triacetic acid functional groups were introduced on the surface of iron oxide NPs by adapting the procedure for the synthesis of ethylene diamine tetraacetic acid (EDTA) from ethylene diamine as described in USPTO 2387735.[37] 200 mg of Fe–Si–diamine NPs were suspended in 100 mL of 10 N KOH and 0.5 g KCN was added. The NPs solution was heated to 60 °C and formaldehyde (HCHO) was added drop by drop under stirring. KCN was in 10% molar excess than HCHO. After 2 hours of stirring at 60 °C, the solution was refluxed overnight. The NPs were magnetically separated and rinsed in 10 N KOH three times. The NPs now had *N*-[(3-trimethoxysilyl) propyl] ethylenediamine triacetic acid tripotassium salt as their surface functional group. The NPs surface was further saturated with *N*-[(3-trimethoxysilyl)propyl]ethylenediamine triacetic acid tripotassium salt to increase solubility and stability [Fe–Si–$(COO^-)_3$ NPs].

The Fe–Si–$(COO^-)_3$ NPs chemical functionality was characterized using FT-IR spectroscopy (Nicolet Magna 760). Briefly, samples were prepared by dropping 100 μl of sample on a ZnSe crystal window and allowed to dry under N_2 flow. SEM samples were prepared by dropping 10 μl of samples on copper strips and allowed to dry under N_2 flow. The SEM samples were imaged with accelerating voltages of 1.3–1.5 keV (Zeiss Merlin). DLS was used to determine nanoparticle size and zeta potential (ζ) in suspension (Brook Haven 90Plus/BI-MAS). Samples for DLS were prepared by mixing 2 μl of nanoparticle solution with 1980 μl of nanopure water.

Synthesis of ^{14}C–Fe–Si–$(COO^-)_3$ NPs

Briefly, 200 mg of Fe–Si–diamine NPs were suspended in 100 mL of 10 N KOH and 1×10^6 nCi $K^{14}CN$ was added. The NPs solution was heated to 60 °C and HCHO was added drop by drop under stirring. $K^{14}CN$ was in 10% molar excess than HCHO. After 2 hours of stirring at 60 °C, the solution was refluxed overnight to yield ^{14}C–Fe–Si–$(COO^-)_3$ NPs. The NPs were magnetically separated, rinsed thrice in 10 N KOH and resuspended in 100 mL of 10 N KOH. The ^{14}C–Fe–Si–$(COO^-)_3$ NPs in 100 mL of 10 N KOH was mixed with 0.5 g KCN and heated to 60 °C. Formaldehyde (HCHO) was added drop by drop to the heated mixture under stirring. KCN was in 10% molar excess than HCHO. This ensured any unreacted amine groups on the surface of the ^{14}C–Fe–Si–$(COO^-)_3$ NPs would be converted to a $–CH_2COO^-$ functional group. After allowing the reaction to proceed overnight, the NPs were rinsed 5 times in milli-Q water and completely dispersed in 100 mL of 90% ethanol 10% water solvent. The NPs surface was further saturated with *N*-[(3-trimethoxysilyl)propyl]ethylenediamine triacetic acid tripotassium salt in to increase solubility and stability [Fe–Si–$(COO^-)_3$ NPs]. After overnight stirring the ^{14}C–Fe–Si–$(COO^-)_3$ NPs were rinsed three times in milliQ water and resuspended in 100 mL of milliQ water. The radioactivity of ^{14}C Fe–Si–$(COO^-)_3$ NPs was measured using TriCarb liquid scintillation counter (Perkin-Elmer). 1 mL of samples solution was added to 20 mL of ultima gold XR liquid scintillation cocktail. 1 mL of supernatant and 1 mL of water were used as control samples. The scintillation count from each vial was integrated over 20 minutes.

Stability of ^{14}C–Fe–Si–$(COO^-)_3$ NPs in physiological medium

The stability of the radioactive labels on ^{14}C Fe–Si–$(COO^-)_3$ NPs was determined in physiologically relevant buffer and serum. Briefly, ^{14}C Fe–Si–$(COO^-)_3$ NPs were suspended in buffer or serum at concentrations comparable to that of the *in vivo* dose to be administered. At 24 hours and 48 hours post incubation the NPs were magnetically separated from the suspension. The NPs free solution was further run through a 0.1 μm filter. The filtered supernatant and a sample of the magnetic NPs were tested for their radioactivity using TriCarb liquid scintillation counter (Perkin-Elmer), as described in the above section. There was only background levels of radioactivity in the supernatant. The difference in radioactivity of the NPs in buffer and serum 24 hours and 48 hours post incu-

bation was not statistically significant enough to be considered a change in radioactivity of the NPs. Hence the radiolabels were considered to be stably linked to the surface of the ^{14}C Fe–Si–$(COO^{-})_3$ NPs even in buffer and serum solutions.

Cell toxicity assays

MTT. 100 μl of 1.5 million cells mL^{-1} C10 lung epithelial cells or RAW 264.7 cells were seeded in each well in a 96 well plate. The cells were allowed to grow for 24 hours in a CO_2 incubator in complete cell culture medium. After 24 hours, the NPs at different concentrations of 10, 20, 50, 100 and 200 μg mL^{-1} was added to each well with triplicates for each concentration. 24 hours after incubation with NPs, MTT assay was used to determine cell viability by assessing mitochondrial respiration.

Intravenous administration of nanoparticles

BALB/c male mice (n = 3) were administered a single intravenous dose of 0.15 mg ^{14}C-labeled iron oxide nanoparticles (Specific Activity tuned to 77.6 nCi mg^{-1}) in 100 μl saline *via* tail vein injection followed by a 50 μl saline flush. Mice were euthanized by CO_2 asphyxiation at specified time points (30 m) and blood and tissues were harvested and stored per the procedure described above. Experiments were conducted following all the guidelines and regulations set by Lawrence Livermore National Laboratory and with Institutional Animal Care and Use Committee (IACUC) approval (protocol#206). The IACUC is a self-regulating body which derives its existence from two sources: (1) the Animal Welfare Act and its amendments, which are administered by the USDA through the Animal and Plant Health Inspection Service (APHIS), and (2) the Health Research Extension Act and its amendments, which are administered by the National Institutes of Health (NIH) through the Office of Laboratory Animal Welfare (OLAW).

Sample collection for AMS analysis

Body weights of each mouse were recorded before and after exposure. At specified time points, each group (n = 3) was euthanized by CO_2 asphyxiation; blood was collected by cardiac puncture and tissues were harvested and stored in glass scintillation vials at −80 °C until analysis. Clean surgical tools were used for each animal to avoid cross contamination. Excised tissues were rinsed twice in phosphate buffered saline (PBS) to remove residual blood before storage. Collected blood was stored in heparinized Microtainer™ tubes (Bectin Dickinson, Franklin Lakes, NJ) and placed on ice until plasma isolation. Plasma was isolated by centrifugation (10 000g for 2 min) and was stored at −80 °C until analysis.

AMS analysis of samples

Tissues were homogenized prior to analysis using a previously established method.[58] Samples were incubated in 1–2 mL of buffer overnight at 37 °C with gentle agitation; after digestion, samples were vortexed to break up the tissue in solution. Plasma was analysed neat, no digestion was necessary. A small aliquot of each sample was used for analysis. Samples were then converted to graphite as previously described and analysed using AMS.[58] The resulting $^{14}C/^{12}C$ ratios obtained by AMS (National Electrostatics Corporation) were converted to ng of nanoparticles per mg of tissue or mL of plasma after subtraction of the background carbon contributed from the sample, and correction for the specific activity, and the carbon content of the sample (10–15% for tissue, 3.8% plasma).[59]

Acknowledgments

This research was supported by the B-FAST, Battelle Center for Fundamental and Applied Systems Toxicology, Multi-Scale Toxicity Initiative. This manuscript has been authored by UT-Battelle, LLC under Contract No. DE-AC05-00OR22725 with the U.S. Department of Energy. Dr. Nallathamby would like to acknowledge material support through proposal #CNMS2013-153, from the Center for Nanophase Materials Sciences, which is sponsored at Oak Ridge National Laboratory by the Division of Scientific User Facilities. We acknowledge the Notre Dame Integrated Imaging Facility (NDIFF) for the use of transmission electron microscopy. Instrument time at NDIIF was funded by Dr. Roeder through NSF DMR-1309587. The United States Government retains and the publisher, by accepting the article for publication, acknowledges that the United States Government retains a non-exclusive, paid-up, irrevocable, world-wide license to publish or reproduce the published form of this manuscript, or allow others to do so, for United States Government purposes. The Department of Energy will provide public access to these results of federally sponsored research in accordance with the DOE Public Access Plan http://energy.gov/downloads/doe-public-access-plan.

Notes and references

1 R. Urso, P. Blardi and G. Giorgi, A short introduction to pharmacokinetics, *Eur. Rev. Med. Pharmacol. Sci.*, 2002, **6** (2–3), 33–44.
2 F. F. Hefti, Requirements for a lead compound to become a clinical candidate, *BMC Neurosci.*, 2008, **9**(Suppl 3), S7.
3 H. Ledford, Drug candidates derailed in case of mistaken identity, *Nature*, 2012, **483**(7391), 519.
4 P. D. Nallathamby, K. J. Lee and X. H. Xu, Design of stable and uniform single nanoparticle photonics for in vivo dynamics imaging of nanoenvironments of zebrafish embryonic fluids, *ACS Nano*, 2008, **2**(7), 1371–1380.
5 A. Astashkina, B. Mann and D. W. Grainger, A critical evaluation of in vitro cell culture models for high-throughput drug screening and toxicity, *Pharmacol. Ther.*, 2012, **134**(1), 82–106.
6 F. P. Guengerich, Mechanisms of drug toxicity and relevance to pharmaceutical development, *Drug Metab. Pharmacokinet.*, 2011, **26**(1), 3–14.

7 J. M. McKim Jr., Building a tiered approach to in vitro predictive toxicity screening: a focus on assays with in vivo relevance, *Comb. Chem. High Throughput Screening*, 2010, **13**(2), 188–206.
8 S. S. Singh, Preclinical pharmacokinetics: an approach towards safer and efficacious drugs, *Curr. Drug Metab.*, 2006, **7**(2), 165–182.
9 T. Maziasz, *et al.*, Predictive toxicology approaches for small molecule oncology drugs, *Toxicol. Pathol.*, 2010, **38**(1), 148–164.
10 M. Z. Ahmad, *et al.*, Metallic nanoparticles: technology overview & drug delivery applications in oncology, *Expert Opin. Drug Delivery*, 2010, **7**(8), 927–942.
11 S. M. Janib, A. S. Moses and J. A. MacKay, Imaging and drug delivery using theranostic nanoparticles, *Adv. Drug Delivery Rev.*, 2010, **62**(11), 1052–1063.
12 D. Yoo, *et al.*, Theranostic Magnetic Nanoparticles, *Acc. Chem. Res.*, 2011, **44**(10), 863–874.
13 P. D. Nallathamby, T. Huang and X. H. Xu, Design and characterization of optical nanorulers of single nanoparticles using optical microscopy and spectroscopy, *Nanoscale*, 2010, **2**(9), 1715–1722.
14 P. D. Nallathamby and X. H. Xu, Study of cytotoxic and therapeutic effects of stable and purified silver nanoparticles on tumor cells, *Nanoscale*, 2010, **2**(6), 942–952.
15 S. K. Nune, *et al.*, Nanoparticles for biomedical imaging, *Expert Opin. Drug Delivery*, 2009, **6**(11), 1175–1194.
16 G. Bao, S. Mitragotri and S. Tong, Multifunctional Nanoparticles for Drug Delivery and Molecular Imaging, *Annu. Rev. Biomed. Eng.*, 2013, **15**(1), 253–282.
17 K. Tsaioun and M. Jacewicz, De-risking drug discovery with ADDME – avoiding drug development mistakes early, *ATLA, Altern. Lab. Anim.*, 2009, **37**(Suppl 1), 47–55.
18 J. Wang and W. Gao, Nano/Microscale motors: biomedical opportunities and challenges, *ACS Nano*, 2012, **6**(7), 5745–5751.
19 J. Leleux and K. Roy, Micro and nanoparticle-based delivery systems for vaccine immunotherapy: an immunological and materials perspective, *Adv. Healthc. Mater.*, 2013, **2**(1), 72–94.
20 S. Singh, Nanomedicine-nanoscale drugs and delivery systems, *J. Nanosci. Nanotechnol.*, 2010, **10**(12), 7906–7918.
21 N. Kamaly, *et al.*, Targeted polymeric therapeutic nanoparticles: design, development and clinical translation, *Chem. Soc. Rev.*, 2012, **41**(7), 2971–3010.
22 K. J. Lee, *et al.*, Study of Charge-Dependent Transport and Toxicity of Peptide-Functionalized Silver Nanoparticles Using Zebrafish Embryos and Single Nanoparticle Plasmonic Spectroscopy, *Chem. Res. Toxicol.*, 2013, **26**(6), 904–917.
23 C. Tang, *et al.*, Concise review: Nanoparticles and cellular carriers-allies in cancer imaging and cellular gene therapy?, *Stem Cells*, 2010, **28**(9), 1686–1702.
24 F. M. Kievit and M. Zhang, Surface engineering of iron oxide nanoparticles for targeted cancer therapy, *Acc. Chem. Res.*, 2011, **44**(10), 853–862.
25 T. Sadhukha, T. S. Wiedmann and J. Panyam, Inhalable magnetic nanoparticles for targeted hyperthermia in lung cancer therapy, *Biomaterials*, 2013, **34**(21), 5163–5171.
26 C. Plank, O. Zelphati and O. Mykhaylyk, Magnetically enhanced nucleic acid delivery. Ten years of magnetofection-progress and prospects, *Adv. Drug Delivery Rev.*, 2011, **63**(14–15), 1300–1331.
27 L. O. Sillerud, *et al.*, SPION-enhanced magnetic resonance imaging of Alzheimer's disease plaques in AbetaPP/PS-1 transgenic mouse brain, *J. Alzheimers Dis.*, 2013, **34**(2), 349–365.
28 A. K. Gupta and M. Gupta, Synthesis and surface engineering of iron oxide nanoparticles for biomedical applications, *Biomaterials*, 2005, **26**(18), 3995–4021.
29 R. Alwi, *et al.*, Silica-coated super paramagnetic iron oxide nanoparticles (SPION) as biocompatible contrast agent in biomedical photoacoustics, *Biomed. Opt. Express*, 2012, **3**(10), 2500–2509.
30 M. Mikhaylova, *et al.*, Superparamagnetism of magnetite nanoparticles: dependence on surface modification, *Langmuir*, 2004, **20**(6), 2472–2477.
31 M. Li, *et al.*, Physiologically based pharmacokinetic modeling of nanoparticles, *ACS Nano*, 2010, **4**(11), 6303–6317.
32 W. I. Hagens, *et al.*, What do we (need to) know about the kinetic properties of nanoparticles in the body?, *Regul. Toxicol. Pharmacol.*, 2007, **49**(3), 217–229.
33 V. B. Mikheev, *et al.*, In vivo inhalation exposures to superparamagnetic iron-oxide nano-particles (SPIONP) followed by magnetic particle detection (MPD) and accelerator mass spectrometry (AMS) analysis, *J. Aerosol Med. Pulm. Drug Delivery*, 2013, **26**(2), A16.
34 J. Mitchell, S. Newman and H. K. Chan, In vitro and in vivo aspects of cascade impactor tests and inhaler performance: a review, *AAPS PharmSciTech*, 2007, **8**(4), E110.
35 C. Dunbar and J. Mitchell, Analysis of cascade impactor mass distributions, *J. Aerosol. Med.*, 2005, **18**(4), 439–451.
36 R. Hanas, L. Lytzen and J. Ludvigsson, Thinner needles do not influence injection pain, insulin leakage or bleeding in children and adolescents with type 1 diabetes, *Pediatr. Diabetes*, 2000, **1**(3), 142–149.
37 F. C. Bersworth, *Method of forming carboxylic amino acids*, 1945, Google Patents.
38 G. C. Kim and W. Kim, Charge-transfer surface complex of EDTA-TiO2 and its effect on photocatalysis under visible light, *Appl. Catal., B*, 2010, **100**(1–2), 77–83.
39 J. Ryczkowski, FT-IR study of the adsorption of some complexones and of EDTA alkaline salts into alumina, *Vib. Spectrosc.*, 2000, **22**(1), 55–62.
40 G. Hasenpusch, *et al.*, Magnetized aerosols comprising superparamagnetic iron oxide nanoparticles improve targeted drug and gene delivery to the lung, *Pharm. Res.*, 2012, **29**(5), 1308–1318.
41 J. M. Hillegass, *et al.*, Assessing nanotoxicity in cells in vitro, *Wiley Interdiscip. Rev.: Nanomed. Nanobiotechnol.*, 2010, **2**(3), 219–231.

42 S. R. Blumen, *et al.*, Unique uptake of acid-prepared mesoporous spheres by lung epithelial and mesothelioma cells, *Am. J. Respir. Cell Mol. Biol.*, 2007, **36**(3), 333–342.
43 R. P. Nishanth, *et al.*, Inflammatory responses of RAW 264.7 macrophages upon exposure to nanoparticles: role of ROS-NFkappaB signaling pathway, *Nanotoxicology*, 2011, **5**(4), 502–516.
44 S. Di Bucchianico, *et al.*, Multiple cytotoxic and genotoxic effects induced in vitro by differently shaped copper oxide nanomaterials, *Mutagenesis*, 2013, **28**(3), 287–299.
45 N. P. Mortensen, *et al.*, Dynamic development of the protein corona on silica nanoparticles: composition and role in toxicity, *Nanoscale*, 2013, **5**(14), 6372–6380.
46 M. Pretze, P. Große-Gehling and C. Mamat, Cross-Coupling Reactions as Valuable Tool for the Preparation of PET Radiotracers, *Molecules*, 2011, **16**(2), 1129–1165.
47 H. Hong, *et al.*, Molecular imaging and therapy of cancer with radiolabeled nanoparticles, *Nano Today*, 2009, **4**(5), 399–413.
48 Y. Liu and M. J. Welch, Nanoparticles labeled with positron emitting nuclides: advantages, methods, and applications, *Bioconjugate Chem.*, 2012, **23**(4), 671–682.
49 K. Greish, G. Thiagarajan and H. Ghandehari, In vivo methods of nanotoxicology, *Methods Mol. Biol.*, 2012, **926**, 235–253.
50 T. Huang, *et al.*, Design and synthesis of single-nanoparticle optical biosensors for imaging and characterization of single receptor molecules on single living cells, *Anal. Chem.*, 2007, **79**(20), 7708–7718.
51 C. Wangler, *et al.*, Click-chemistry reactions in radiopharmaceutical chemistry: fast & easy introduction of radiolabels into biomolecules for in vivo imaging, *Curr. Med. Chem.*, 2010, **17**(11), 1092–1116.
52 R. Rossin, *et al.*, 64Cu-labeled folate-conjugated shell cross-linked nanoparticles for tumor imaging and radiotherapy: synthesis, radiolabeling, and biologic evaluation, *J. Nucl. Med.*, 2005, **46**(7), 1210–1218.
53 F. Staud, *et al.*, Disposition of radioactivity after injection of liver-targeted proteins labeled with 111In or 125I. Effect of labeling on distribution and excretion of radioactivity in rats, *J. Pharm. Sci.*, 1999, **88**(6), 577–585.
54 G. A. Bailey, *et al.*, H(2)azapa: a Versatile Acyclic Multifunctional Chelator for (67)Ga, (64)Cu, (111)In, and (177)Lu, *Inorg. Chem.*, 2012, **51**(22), 12575–12589.
55 M. Longmire, P. L. Choyke and H. Kobayashi, Clearance properties of nano-sized particles and molecules as imaging agents: considerations and caveats, *Nanomedicine*, 2008, **3**(5), 703–717.
56 M. T. Zhu, *et al.*, Particokinetics and extrapulmonary translocation of intratracheally instilled ferric oxide nanoparticles in rats and the potential health risk assessment, *Toxicol. Sci.*, 2009, **107**(2), 342–351.
57 J. D. Slack, *et al.*, Acute hemodynamic effects and blood pool kinetics of polystyrene microspheres following intravenous administration, *J. Pharm. Sci.*, 1981, **70**(6), 660–664.
58 M. A. Malfatti, *et al.*, Determining the pharmacokinetics and long-term biodistribution of SiO2 nanoparticles in vivo using accelerator mass spectrometry, *Nano Lett.*, 2012, **12**(11), 5532–5538.
59 J. S. Vogel and A. H. Love, Quantitating isotopic molecular labels with accelerator mass spectrometry, *Methods Enzymol.*, 2005, **402**, 402–422.